A 92.3%-Efficiency Switching-Mode Dual-Output Regulating Rectifier With Improved Link Adaptability for Wireless Power Transfer

Lu, Tianqi; Du, Sijun

DOI
10.1109/JSSC.2025.3540596

Publication date
2025

Document Version
Final published version

Published in
IEEE Journal of Solid-State Circuits

A 92.3%-Efficiency Switching-Mode Dual-Output Regulating Rectifier With Improved Link Adaptability for Wireless Power Transfer

Tianqi Lu, *Graduate Student Member, IEEE*, and Sijun Du, *Senior Member, IEEE*

***Abstract*— This article presents a 6.78-MHz switching-mode wireless power transfer (WPT) receiver (RX) with single-stage dual-output regulation and improved adaptability to link variations for biomedical applications. Based on a modified voltage doubler topology, it optimally transitions between voltage mode (VM) and resonant current mode (RCM) to extend the WPT range without compromising efficiency or delivered power. Seamless mode transition is achieved with no dead zones or output undershoots, thanks to the proposed quasi-open-circuit mode detection leveraging existing operational states without power-carrier interferences. The essential advantages of switching mode are consolidated via transient modeling. To meet dual-voltage-domain supply requirement in bio-implants, the RX uses stacked dc nodes in the voltage doubler to generate two regulated outputs with only three power switches. Designed and fabricated in a 180-nm CMOS technology, the proposed RX regulates two dc outputs at 1.8 and 3.3 V, respectively, with unobservable load-transient over/undershoots and cross-regulations. Using a 3.3-V-supplied class-D transmitter (TX), a 13.5-mm-radius TX coil, and an 11.5-mm-radius RX coil, the RX achieves a maximum WPT range of 7.5 cm under both 50-kΩ load conditions, demonstrating a 42% extension compared with VM-only operation. Real-time mode transition is validated through coil separation distance transients between 3 and 5.5 cm. In addition, with adaptive delay compensation in both VM and RCM operations, the RX achieves a peak power conversion efficiency (PCE) of 92.3% at a maximum output power of 171 mW.**

***Index Terms*— Dual output, link adaptive, receiver (RX), regulating rectifier, resonant current mode (RCM), soft switching, switching mode, voltage mode (VM), wireless power transfer (WPT).**

I. Introduction

WIRELESS power transfer (WPT) is a promising non-invasive solution for powering implantable medical devices (IMDs) such as retinal prostheses, neural interfaces, and brain implants [1]. In such applications, the inductive link coupling condition often fluctuates due to relative movements between the transmitter (TX) and the receiver (RX) coils [2], [3], [4], as shown in Fig. 1. In addition, IMD systems typically require two distinct power supplies, in which the lower one is for signal processing circuits and the higher one is for electrical stimulation and high-performance analog front-ends [3], [5], [6].

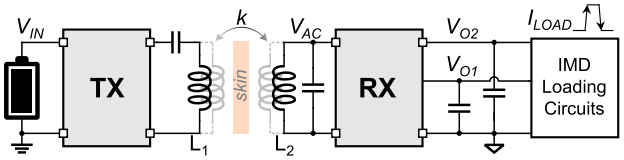

Fig. 1. Typical structure of a biomedical WPT system facing variable inductive link.

To ensure reliable power delivery against coupling variations in a WPT system, a third intermediate coil can be implemented between TX and RX coils to concentrate magnetic flux [7], [8]; however, this significantly increases the system complexity and fabrication cost. In typical two-coil systems, a parallel-resonant LC tank is usually deployed at the RX side to achieve a high voltage conversion ratio (VCR) over the link (Fig. 1). In that case, the RX coil inductance is preferably sized large to facilitate a high VCR [9], [10]. Nonetheless, as an implant, the stringent size requirement for RX results in a low quality factor of the RX coil, leading to high conduction loss and local tissue overheating risk.

Besides the resonant link, a typical two-stage RX interface circuit comprises an open-loop voltage-mode (VM) rectifier, such as a full-bridge rectifier or a voltage doubler, followed by a dc–dc converter for voltage regulation [11], [12], [13], as shown in Fig. 2(a). The dc–dc converter can provide tight voltage regulation and a high VCR with a boost topology. However, both the rectifier and dc–dc converter introduce power losses, degrading the total power conversion efficiency (PCE). It also necessitates extra power components.

To address cascaded losses and save components, single-stage regulating rectifiers have been developed in the past decade, of which most are based on full-bridge structures [14], [15], [16], as shown in Fig. 2(b). The in situ rectifier output voltage regulation can be achieved by hysteresis-based pulse-frequency modulation [15], [17], [18], pulsewidth modulation [19], [20], pulse conduction-time modulation [21], [22], etc. Thanks to the simplified power paths, high PCE (over 90%) can be achieved. Nevertheless, the VCR of RX is limited to the inherent voltage gain of the rectifier topology. In the case of a full-bridge rectifier, the VCR is smaller than 1. Hence, the rectifier only conducts when the input amplitude exceeds the output voltage, setting a high power threshold. To mitigate this issue, regulating voltage doubler with a theoretical VCR

Received 22 November 2024; revised 12 January 2025; accepted 4 February 2025. Date of publication 3 March 2025; date of current version 1 July 2025. This article was approved by Associate Editor Yang Zhang. *(Corresponding author: Sijun Du.)*

The authors are with the Department of Microelectronics, Delft University of Technology, 2628 CD Delft, The Netherlands (e-mail: sijun.du@tudelft.nl).

Color versions of one or more figures in this article are available at https://doi.org/10.1109/JSSC.2025.3540596.

Digital Object Identifier 10.1109/JSSC.2025.3540596

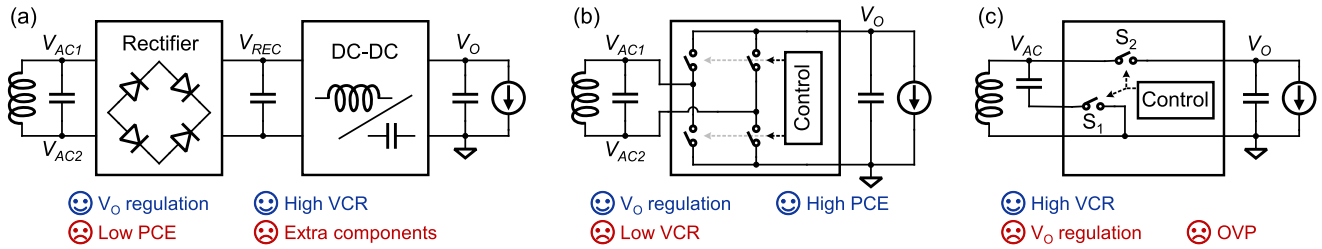

Fig. 2. Typical RX topologies. (a) Two-stage RX including a rectifier and a dc–dc converter. (b) Single-stage regulating rectifier RX. (c) RCM rectifier RX.

of 2 has been presented [17], [23]. Unfortunately, the doubling effect can gradually diminish when the link coupling becomes weaker, because of the reflected impedance difference between a full-bridge rectifier and a voltage doubler [23], [24].

To break through the VCR limitation of VM topologies, resonant current-mode (RCM) rectifiers have been proposed [25], [26], [27], as illustrated in Fig. 2(c). Similar to a boost converter, the LC resonant tank at RX is first resonating for multiple periods with the switch S_1 closed; then, the accumulated energy is delivered to the output at once using the RX coil as a current source by closing S_2. Thanks to this principle, the RX can deliver power as long as the accumulated resonance energy is higher than power dissipation, significantly lowering the power threshold and boosting the VCR. A three-phase RCM rectifier was recently presented with a freewheeling phase, allowing power-efficient in situ output voltage regulation [28]. Unfortunately, though an RCM rectifier improves weak-coupling performance by multi-period resonance, the lower charging frequency induces a larger steady-state output voltage ripple, and the resonance phase poses over-voltage risks under strong-coupling conditions. Series-LC-based RCM topologies avoid the over-voltage risk, but they suffer from either high conduction loss caused by energy residual [3] or complex closed-loop control of phase switching, vulnerable to coupling fluctuations [26].

To combine the advantages of both VM and RCM topologies, a reconfigurable voltage-/current-mode (VCM) rectifier was presented in [29]. A half-bridge rectifier was designed to be capable of reconfiguring between VM and RCM operations, given their topology similarity. However, a dead zone between the VM and RCM was exposed due to the lack of effective input power detection at RX [30]. A modified operation was introduced in [31] to solve the dead zone issue by frequently switching between VM and RCM with an unalterable pattern, which sub-optimizes the strong-coupling operation. Moreover, the half-bridge topology limits the output power and PCE. To address this, a hybrid VCM rectifier was proposed with a full-wave operation [32], [33]. However, it will not enter RCM until a huge voltage drop presents at the output, and it switches back to VM as long as the output voltage is recovered regardless of the input power level. The invisible VM under weak coupling rather accelerates the output voltage dropping, resulting in large ripples and unnecessary power losses.

In this article, a switching-mode RX is proposed to seamlessly select the optimal mode between VM and RCM against link variations without transition issues such as dead zone or output undershoots [34]. Unlike previous VCM rectifiers,

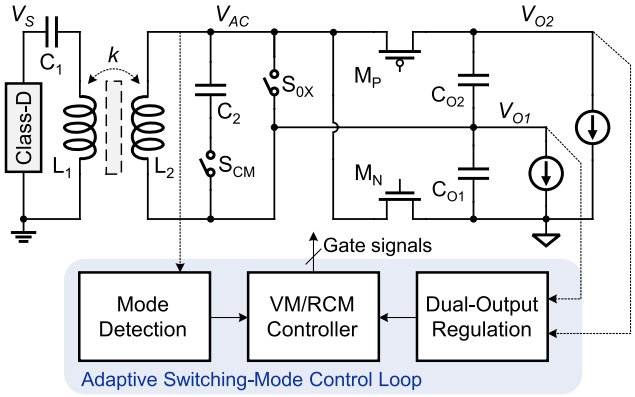

Fig. 3. Proposed WPT system with the link-adaptive SMDOR.

accurate mode transition is achieved based on the proposed quasi-open-circuit mode detection technique in both VM and RCM. A modified dual-output voltage doubler topology enables single-stage dual-output regulation using only three power switches and one freewheeling switch. To illuminate the VCR improvement by RCM and showcase the appropriate mode transition point, the proposed RX transient behavior has been precisely modeled, which is verified by simulations and measurements. The remainder of this article is structured as follows. Section II presents the topology, modeling, and operational principle of the proposed RX. Section III shows the system and circuit implementations. Section IV demonstrates measurement results, and Section V draws conclusions.

II. Proposed Switching-Mode Rectifier

Fig. 3 presents the proposed WPT system with the link-adaptive switching-mode dual-output regulating rectifier (SMDOR). SMDOR involves three power switches: S_{CM}, M_P, and M_N. The switches M_P and M_N form a dual-output voltage doubler with two output capacitors C_{O1} and C_{O2}. The switch S_{CM} connects the resonating capacitor C_2 in series, enabling the RCM operation by disconnecting C_2 when the RX coil L_2 works as a current source. During the VM operation, S_{CM} keeps closed with a considerably large switch size to minimize its conduction loss; during the RCM operation, a smaller size of S_{CM} is used to minimize the switching loss. The switch S_{0X} connects the two ac input terminals to enable a freewheeling mode. In the proposed adaptive switching-mode control loop, the input voltage, V_{ac}, is selectively monitored by the mode detection block, and the dual-output regulation block determines the proper operation state in both VM and RCM,

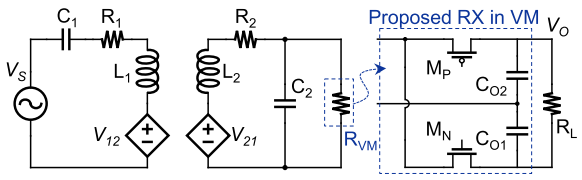

Fig. 4. Modeling of the proposed RX VM operation.

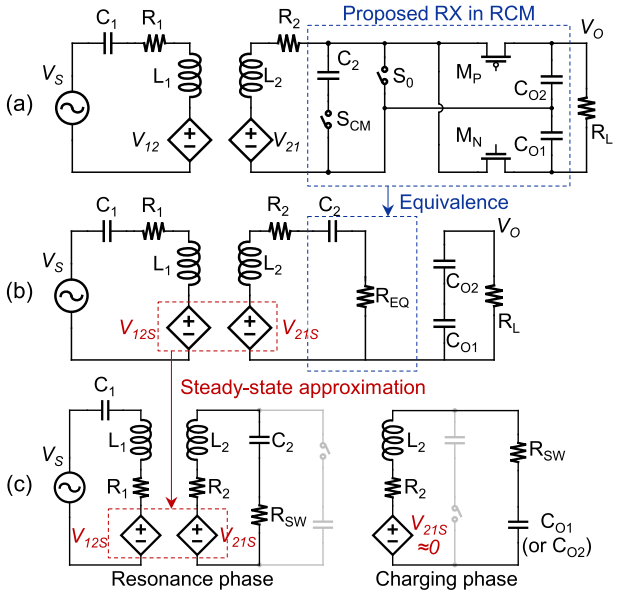

Fig. 5. Modeling of the proposed RX RCM operation. (a) Schematic. (b) RX RCM operation equivalence. (c) TX steady-state approximation.

to regulate the two dc outputs, V_{O1} and V_{O2}. Based on both input and output information, the VM/RCM controller finalizes the gate driving signals with adaptive delay compensation facilitating soft switching.

A. Switching-Mode Modeling and Analysis

The essential advantages of switching mode should be illuminated in theory. As shown in Fig. 4, the proposed RX in VM is modeled as a typical voltage doubler excluding output regulation. Derived from [9] and [10], the VM VCR, defined as the ratio between V_O and $|V_S|$, is given by

$$\mathrm{VCR_{VM}} = \frac{\sqrt{P_{\mathrm{TX}} \cdot \eta_{\mathrm{LINK}}\ \eta_{\mathrm{VM}} \cdot R_L}}{|V_S|} \tag{1}$$

where η_{VM} is the VM RX PCE. Assuming perfect impedance matching at both TX and RX by L_1–C_1 and L_2–C_2 networks, the TX power from V_S, P_{TX}, and the link efficiency, η_{LINK}, can be, respectively, expressed as

$$P_{\mathrm{TX}} = \frac{|V_S|^2}{2(R_1 + R_{\mathrm{EQVM}})} \tag{2}$$

$$\eta_{\mathrm{LINK}} = \frac{R_{\mathrm{EQVM}}}{(R_{\mathrm{EQVM}} + R_1) \cdot [R_2 R_{\mathrm{VM}} (\omega C_2)^2 + 1]} \tag{3}$$

where the input resistance of the VM RX, R_{VM}, and the equivalent resistance of the VM RX reflected at TX, R_{EQVM}, are, respectively, given by

$$R_{\mathrm{VM}} = \frac{R_L \cdot \eta_{\mathrm{VM}}}{2 \cdot \mathrm{VCR_{VD}^2}} = \frac{R_L \cdot \eta_{\mathrm{VM}}}{8} \tag{4}$$

TABLE I
MODELING AND SIMULATION CIRCUIT PARAMETERS

Parameter		Value
Carrier frequency, f_0 ($1/P_0$)		6.78 MHz
Excitation amplitude, $\lvert V_S \rvert$		5 V
TX coil	inductance, L_1	1 μH
	resistance, R_1	0.5 Ω
	outer radius, r_1	13.5 mm
RX coil	inductance, L_1	300 nH
	resistance, R_2	2 Ω
	outer radius, r_2	10 mm
Switch on resistance, R_{SW}		0.1 Ω
Output capacitance, C_{O1} and C_{O2}		10 nF

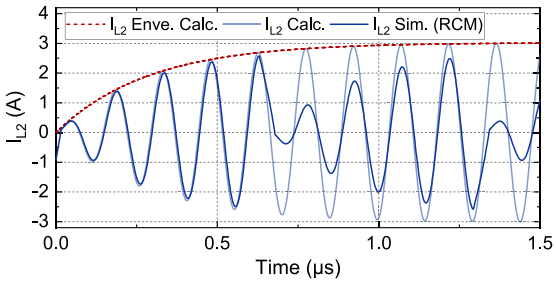

Fig. 6. Modeled and simulated transient waveforms of I_{L2} in the RCM RX at coupling factor $k = 0.05$.

$$R_{\mathrm{EQVM}} = \frac{\omega^2 M^2 R_{\mathrm{VM}} (\omega C_2)^2}{R_2 R_{\mathrm{VM}} (\omega C_2)^2 + 1} \tag{5}$$

where $\mathrm{VCR_{VD}}$ is the inherent VCR of voltage doubler; $\omega = 2\pi f_0$ is the angular frequency of the carrier ($f_0 = 6.78$ MHz); and M is the mutual inductance between the TX and RX coils. Note that $(\omega C_2 R_L)^2 \gg 1$ is assumed to derive R_{EQVM} in (5). This neglects the effect of R_L on resonance shift, which should also be practically satisfied by a parallel-resonant RX [9].

Fig. 5 shows the modeling of the proposed RX when it is in RCM. Briefly, the RCM RX has two operational phases: resonance phase and charging phase, excluding output regulation. In the resonance phase, L_2–C_2 tank is freely resonating via $\mathrm{S_{CM}}$; in the charging phase, L_2 becomes a current source delivering the resonance energy to one of the output capacitors, C_{O2} (or C_{O1}), via M_P (or M_N).

In previous RCM analysis in [27], [29], and [35], the TX's steady state is approximated solely based on the impedance reflection during the resonance phase considering its much larger duty ratio. This might be validated under extremely weak coupling conditions with a low-quality TX resonance loop ($R_1 = 30\ \Omega$ in [27] and [35]), in which the RX transients are nearly invisible. However, it easily loses the efficacy in practical WPT scenarios with higher power levels.

In this article, energy conservation is relied on to approximate the TX's steady state with a proposed time-domain averaged RCM-equivalent resistance, R_{EQ}, as shown in Fig. 5(b). Since the RCM operation will only engage under weak coupling conditions, this approximation helps provide intuitive conclusions without solving time-dependent resonance transients at TX. Then, based on the approximated TX steady state, the two-phase RCM transient behavior can be solved at RX, regarded as a series-RLC resonant circuit. The final RCM model is displayed in Fig. 5(c).

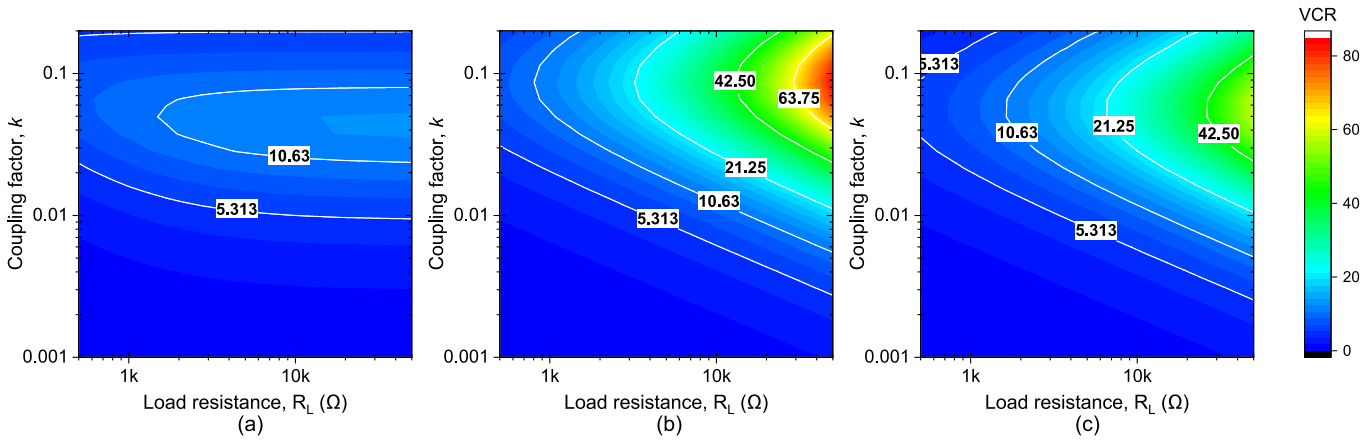

Fig. 7. Modeled VCR colormaps versus load resistance, R_L, and coupling factor, k. (a) VM RX. (b) RCM RX with the resonance phase duration of $1.5 \times P_0$. (c) RCM RX with the resonance phase duration of $4.5 \times P_0$.

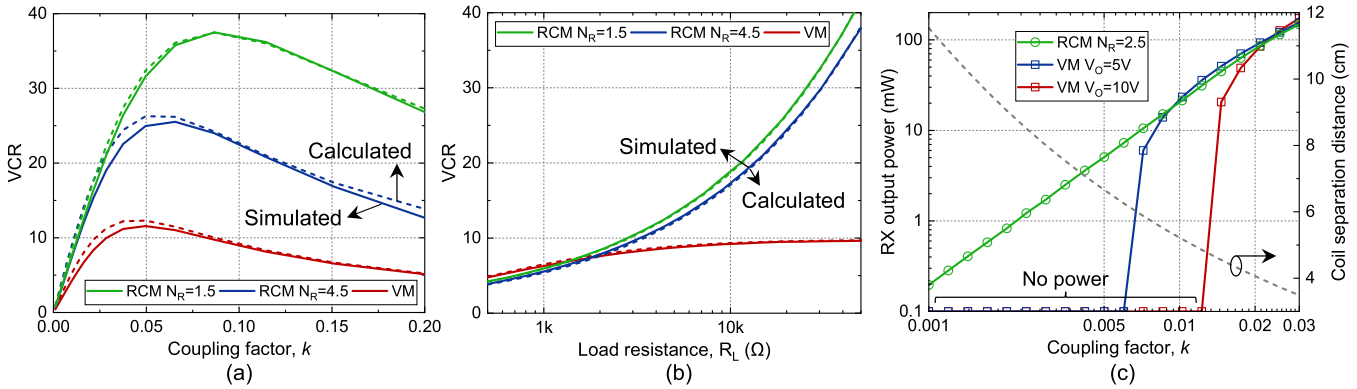

Fig. 8. Modeled and simulated VCR comparisons between VM and RCM. (a) VCR versus k at $R_L = 10$ kΩ. (b) VCR versus R_L at $k = 0.025$. (c) Simulated RX output power versus k at $|V_S| = 1.8$ V with constant-V_O loads.

In the resonance phase of the RCM RX, if all the resonance energy in the previous cycle has been delivered to the output, the L_2–C_2 tank starts with zero initial conditions. For efficient WPT, the RX during resonance phase shows an underdamped response. Given $V_{21}(t) = |V_{21}|\sin(\omega t)$, the inductor current I_{L2} can be expressed as

$$I_{L2}(t) = I_{\text{MAX}}(1 - e^{-\alpha t})\sin(\omega t) \tag{6}$$

where the damping factor α and the steady-state peak current I_{MAX} are, respectively, given by

$$\alpha = \frac{R_2 + R_{\text{SW}}}{2L_2}; \quad I_{\text{MAX}} = \frac{|V_{21}|}{R_2 + R_{\text{SW}}} \tag{7}$$

in which R_{SW} is the switch ON-resistance. At RX, the input power, $P_{\text{IN,RX}}$, can be separated into the output power of the resonance phase, P_{OUT}, and the loop power dissipation during both the resonance and charging phases, P_{LOSS}. Here, it assumes that the RX in the charging phase is far OFF-resonance and thus has negligible power received from the TX. If the resonance phase duration is set to $T_{\text{RES}} = ((N - 0.5)/2f_0)$ (or $((N - 0.5)/2)P_0$, N is integral) and the charging phase always starts at I_{L2}-peak moments, P_{OUT} and P_{LOSS} can be, respectively, derived as

$$P_{\text{OUT}} = \frac{E_{L2}}{T_{\text{RES}} + \frac{0.25}{f_0}} = \frac{L_2 I_{L2}^2(T_{\text{RES}})}{2\left(T_{\text{RES}} + \frac{0.25}{f_0}\right)} \tag{8}$$

$$P_{\text{LOSS}} = \frac{R_2 + R_{\text{Sw}}}{T_{\text{RES}} + \frac{0.25}{f_0}} \int_0^{t_{\text{RES}} + \frac{0.25}{f_0}} I_{L2}^2(t)\, dt \tag{9}$$

where I_{L2} during the charging phase is approximated to keep a sinusoidal waveform and the charging phase duration is about $(0.25/f_0)$. To further calculate P_{OUT} for VCR, $V_{21}(t)$ needs to be solved to find $I_{L2}(t)$. Applying Kirchhoff's voltage law (KVL) at the TX loop and RX loop in the resonance phase results in

$$\left(j\omega L_1 + R_1 + \frac{1}{j\omega C_1}\right) I_{L1}(t) + V_{12}(t) = V_S(t) \tag{10}$$

$$\left(j\omega L_2 + R_2 + R_{\text{SW}} + \frac{1}{j\omega C_2}\right) I_{L2}(t) = V_{21}(t). \tag{11}$$

At resonance where $\omega = (1/(L_1C_1)^{1/2}) = (1/((L_2C_2)^{1/2}))$, the amplitude of $V_{21}(t)$ can be given by

$$|V_{21}| = \omega M |I_{L1}| = \omega M \frac{|V_S|}{R_1 + R_{\text{EQCM}}} \tag{12}$$

where the equivalent resistance of the RCM RX reflected at TX, R_{EQCM}, can be derived as

$$R_{\text{EQCM}} = \frac{\omega^2 M^2}{R_2 + R_{\text{EQ}}} \tag{13}$$

in which R_{EQ} is the proposed RCM-equivalent resistance. On the other hand, the input power of RX, $P_{\text{IN,RX}}$, can be

expressed as

$$P_{\mathrm{IN,RX}} = \frac{|V_S|^2}{2(R_1 + R_{\mathrm{EQCM}})} \cdot \frac{R_{\mathrm{EQCM}}}{R_1 + R_{\mathrm{EQCM}}}. \tag{14}$$

Based on the relationship that $P_{\mathrm{IN,RX}} = P_{\mathrm{OUT}} + P_{\mathrm{LOSS}}$, R_{EQ} can be obtained by simultaneously solving (8), (9), and (14). Then, P_{OUT} can be calculated to reveal VCR by

$$\mathrm{VCR_{CM}} = \frac{\sqrt{P_{\mathrm{OUT}} \cdot \eta_{\mathrm{CM}} \cdot R_L}}{|V_S|} \tag{15}$$

where η_{CM} is the RCM RX PCE excluding conduction losses, which are already considered in P_{LOSS}.

Cadence simulations are conducted to verify the efficacy of this RCM modeling. Table I shows the circuit parameters used in both modeling and simulations. Fig. 6 presents both the simulated I_{L2} waveform using the proposed RCM RX topology and the modeled (calculated) I_{L2} transient waveform. It is observed that the RCM resonance phase can be accurately mimicked by the series-RLC start-up transient, and the calculated envelope curve ($|I_{L2}|$ in the modeling) tightly tracks the peak I_{L2} values in the simulation.

Fig. 7 shows the VCR performance of both VM and RCM RX based on the aforementioned models, using the parameters from Table I and $\eta_{\mathrm{VM}} = \eta_{\mathrm{CM}} = 1$. As shown in Fig. 7(a), the VM RX shows limited VCR whose maximum only reaches around 10, at the critical coupling $k = 0.05$ (maximum power point), over the entire R_{L} range from 500 Ω to 50 kΩ. The VM VCR drops below 5 when k falls below 0.01. In comparison, the RCM RX shows a much higher VCR in general. Fig. 7(b) shows the RCM RX performance when the resonance phase duration is $1.5 \times P_0$. The maximum VCR exceeds 80 at the critical coupling $k = 0.08$, and the VCR remains higher than 5 even when k drops to 0.003 at $R_{\mathrm{L}} = 50$ kΩ. Fig. 7(c) shows the RCM RX with a $4.5 \times P_0$ resonance phase duration and a critical coupling $k = 0.055$ similar to the VM RX. Due to higher P_{LOSS} in the resonance phase, it shows lower VCR under strong coupling conditions; its weak-coupling VCR is comparable to the $1.5 \times P_0$ RCM case. Note that with a higher quality RX coil, the RCM operation can potentially show a higher weak-coupling VCR with a longer resonance phase.

Fig. 8 shows comparison of the VCR of VM and RCM RX via both the models and simulations. It is observed from Fig. 8(a) that the RCM VCR can outperform VM VCR over the entire k range from 0.001 to 0.02 at $R_{\mathrm{L}} = 10$ kΩ. In the weaker coupling region, the RCM RX can still present at least doubled VCR than the VM RX. The calculated results from models show good fits with the simulated results; the small error is mainly caused by the impedance matching approximation during the modeling process. Fig. 8(b) shows the relationship between VCR and R_{L} at $k = 0.025$. Under this coupling condition, the VM RX slightly outperforms the RCM RX when a heavy load condition applies ($R_{\mathrm{L}} <$ 2 kΩ). However, the RCM RX fast boosts the VCR when R_{L} increases, which will not be limited by its circuit topology. This endorses the potential that the proposed RX can sustain the output voltage by switching to RCM operation and, in case of a very weak inductive link, simultaneously lightening its load condition (e.g., putting some loads into sleep).

Besides the open-loop VCR analyses, Fig. 8(c) displays the relationship between the RX output power and k when the RX has a constant-output-voltage load, mimicking a regulating rectifier. The amplitude of the source voltage, $|V_S|$, is set to 1.8 V, closely matching IMD power levels. Since the constant output voltage, V_{O}, sets a "conducting" threshold for the VM rectifier, the VM RX cannot harvest power from TX until k exceeds 0.007 (or 0.012) at $V_{\mathrm{O}} = 5$ V (or 10 V). In contrast, the RCM RX can always harvest power from TX insensitive to k, thanks to its current-mode nature, thus achieving an extended operable coupling range. Based on the coil sizes in Table I, the coil separation distance, D_{12}, can be approximated using the equation [9]

$$D_{12} = \sqrt{\left(\frac{r_1^2 \cdot r_2^2}{k \cdot \sqrt{r_1 \cdot r_2}}\right)^{\frac{2}{3}} - r_1^2} \tag{16}$$

to provide a more intuitive feeling of the extension feature. For miniaturized IMD applications with a smaller or higher resistance RX coil, the RCM operation promises an even more significant extension of the WPT range.

B. Operational States of SMDOR

Fig. 9 shows the operational modes and states of the proposed SMDOR. It has three operational modes: VM, RCM, and freewheeling (0X) mode. In either VM or RCM, it, respectively, presents three different operational states to realize the dual-output power distribution. In RCM, each state further involves two phases: a resonance phase and a charging phase. The detailed operation is as follows.

1) VM Operation: When the inductive link provides the RX with sufficient power, and the outputs also demand power, the proposed RX operates in VM. Herein, $\mathrm{S_{CM}}$ is always ON, and $\mathrm{S_{0X}}$ is always OFF. L_2 and C_2 form a parallel resonance tank at RX with a dual-output voltage doubler load. If both the outputs demand power, the RX works in state $\mathrm{S_{VM1}}$, where both M_{P} and M_{N} are enabled as active diodes. The received power is split and then delivered to both C_{O1} and C_{O2}. If V_{O1} is sufficiently high while V_{O2} is not, the RX will switch to state $\mathrm{S_{VM2}}$, where only M_{P} remains as an active diode. Hence, the low side of the voltage doubler is disabled, and all the received power flows to C_{O2} to level up V_{O2}. In the opposite case, the RX enters state $\mathrm{S_{VM3}}$ to only charge C_{O1}. Though V_{O2} might also increase in this state due to capacitor stacking, the proper voltage level can still be maintained by tight regulation settings, which will be verified in Sections III and IV.

2) RCM Operation: When the inductive link weakens, the RX switches to RCM to maximize power receiving from the link. $\mathrm{S_{0X}}$ still maintains OFF in this mode. A complete RCM cycle includes a resonance phase and a charging phase. In the resonance phase Φ_1, $\mathrm{S_{CM}}$ is ON, and both M_{P} and M_{N} are disabled. Hence, the received energy is accumulated in the L_2–C_2 resonant tank. The charging phase starts when the absolute current in L_2 reaches its maximum, indicating that L_2 holds all the resonance energy, and ends when I_{L2} returns to zero. The direction of I_{L2} should match the output to be charged. To charge C_{O2}, the phase Φ_2 is entered to turn off $\mathrm{S_{CM}}$ and turn

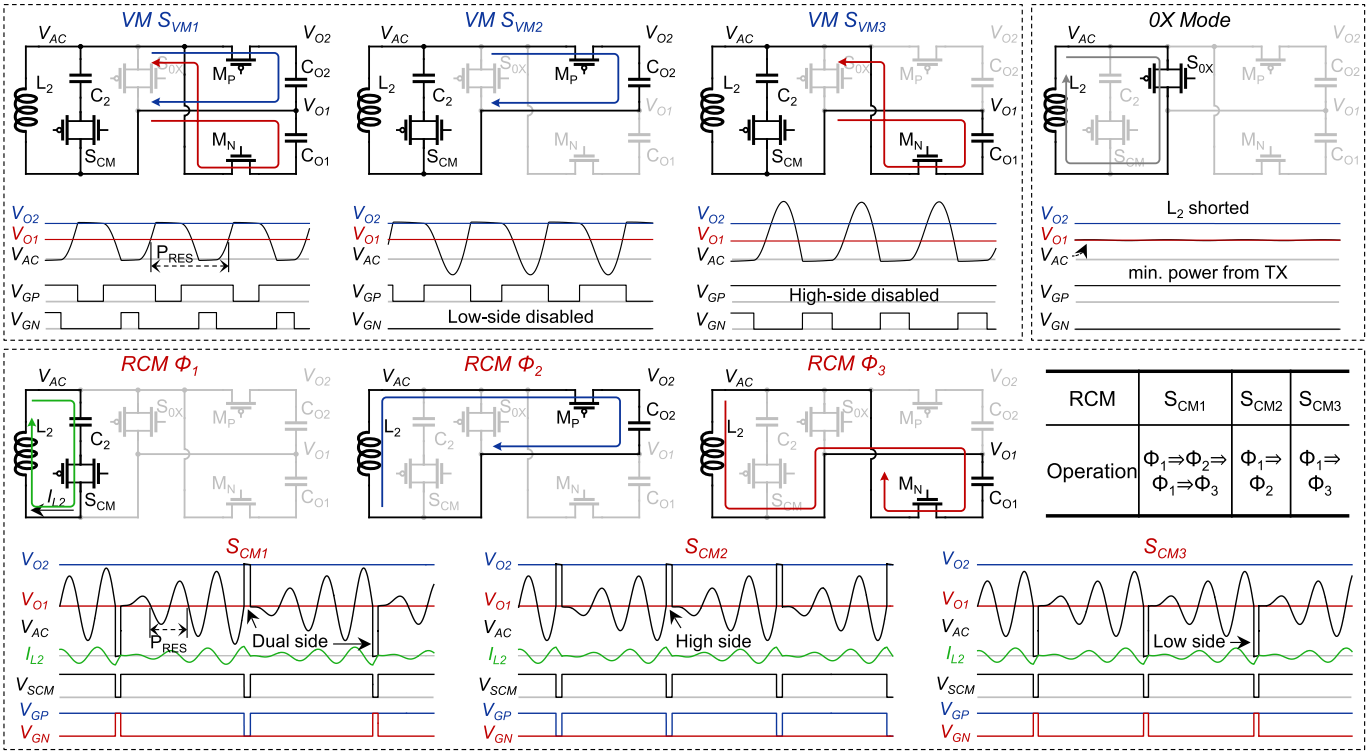

Fig. 9. Operational modes and states of the proposed SMDOR.

on M_P when I_{L2} reaches the positive peak. Similarly, to charge C_{O1}, the phase Φ_3 is entered, starting with a negatively peak of I_{L2}. The waveforms of three RCM states are shown in Fig. 9 (bottom). If both the outputs require power, the RX operates in state S_{CM1} to charge C_{O1} and C_{O2} in an alternate manner of $\Phi_1 \rightarrow \Phi_2 \rightarrow \Phi_1 \rightarrow \Phi_3$. In contrast, it enters state S_{CM2} ($\Phi_1 \rightarrow \Phi_2$) or state S_{CM3} ($\Phi_1 \rightarrow \Phi_3$) when power is in demand for only C_{O2} or C_{O1}.

3) Freewheeling (0X) Mode: A freewheeling (0X) mode is necessary to idle the RX when both the outputs have sufficient energy in the reservoir capacitors. In the 0X mode, only the switch S_{0X} is on. Hence, L_2–C_2 resonance is shorted by the low impedance path S_{0X}, minimizing the power received from the link. Furthermore, since this 0X mode changes the reflected impedance of RX at the TX side, it inherently sends an impedance-shift-keying signal to TX, which can be demodulated by TX to stop emitting power and thus improving end-to-end efficiency of the whole WPT system.

III. System Implementations

Fig. 10 illustrates the system diagram of the proposed SMDOR. In the power stage, S_{CM} and S_{0X} are implemented by transmission gates. The three power switches, S_{CM}, M_P, and M_N, are adaptively sized for VM and RCM operations to optimize the efficiency tradeoff. M_P, M_N, and S_{0X} have dynamic body biases (DBBs), which provide p- and n-type MOSFET devices with the maximum and minimum voltages, V_{MAX} and V_{MIN}, respectively. In addition, M_P, M_N, and S_{0X} have adaptive gate biases to isolate large voltage swings during their OFF states, allowing dual-output regulation, which will be detailed in Section III-C. In the control circuitry, both V_{O1} and V_{O2} are monitored in the dual-output controller using a parallel pulse-frequency modulation (PPFM) strategy, to be revealed in Section III-A. The ac input voltage, V_{ac}, is monitored in the mode detector at selected moments, determined by the detection trigger, which will be shown in Section III-B. Based on the mode signal V_{MODE}, the gate signals of M_P and M_N, V_{GP} and V_{GN}, are generated by either VM or RCM switching control loop, both of which have adaptive delay compensation to achieve soft switching, as shortly discussed in Section III-C.

A. Dual-Output Regulation

Fig. 11 shows the dual-output regulation waveforms of SMDOR in RCM under I_{LOAD2} load transient, and the implementations of the hysteresis comparators. The lower output voltage, V_{O1}, is regulated to stay in a predetermined hysteresis window through adjusting the ON/OFF duty cycle of M_N by the control signal V_{CTN}. Then, by referring V_{O1} as a dc reference, the higher output voltage, V_{O2}, is regulated by controlling the ON/OFF duty cycle of M_P by the control signal V_{CTP}, also based on a hysteresis window. Hence, both the outputs are regulated in a parallel way without power distribution conflicts; different ON/OFF states of M_P and M_N result in multiple operational states described in Section II-B. In practice, the ripple in V_{O1} can be regarded as a common-mode drift for V_{O2}, resulting in a slightly larger ripple in V_{O2} compared with its preset hysteresis window. However, given programmable hysteresis windows, the output ripples can still be application-dependently specified and designed. Both VM and RCM SMDOR regulate the two outputs in the same way, as shown in Fig. 11 [23].

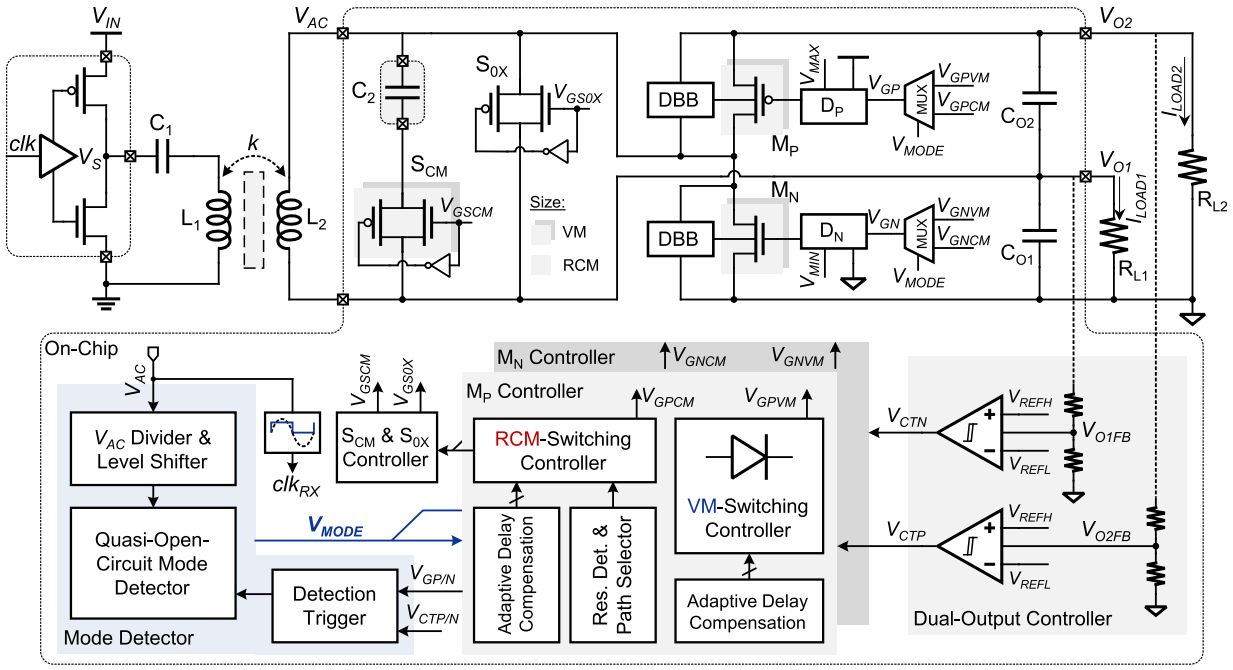

Fig. 10. System diagram of the proposed SMDOR.

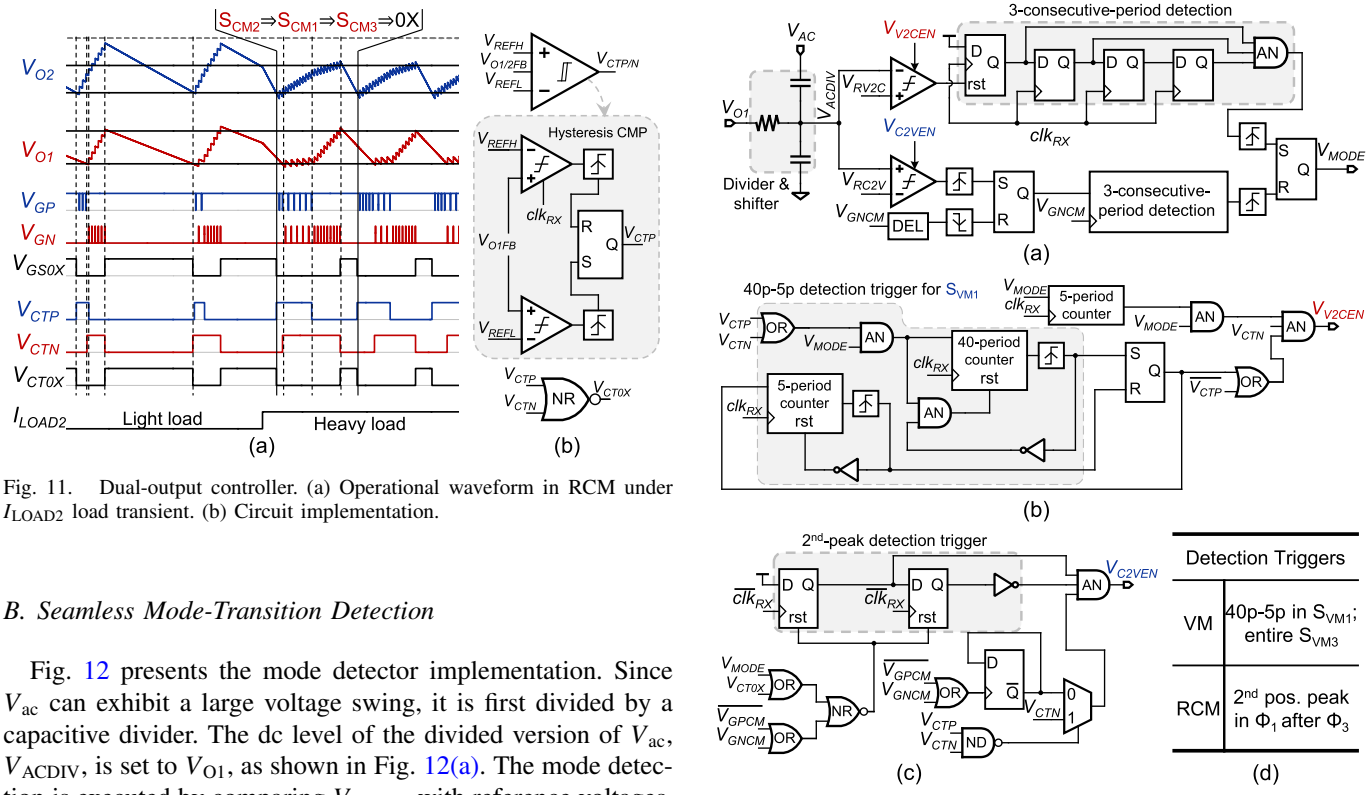

Fig. 11. Dual-output controller. (a) Operational waveform in RCM under I_{LOAD2} load transient. (b) Circuit implementation.

Fig. 12. Mode detector implementation. (a) Quasi-V_{ac}-open-circuit detector. (b) Mode detection trigger in VM. (c) Mode detection trigger in RCM. (d) Trigger summary.

B. Seamless Mode-Transition Detection

Fig. 12 presents the mode detector implementation. Since V_{ac} can exhibit a large voltage swing, it is first divided by a capacitive divider. The dc level of the divided version of V_{ac}, V_{ACDIV}, is set to V_{O1}, as shown in Fig. 12(a). The mode detection is executed by comparing V_{ACDIV} with reference voltages, V_{RV2C} and V_{RC2V}, in two continuous-time comparators with enable signals, V_{V2CEN} and V_{C2VEN}, respectively. The reference voltages determine the mode transition points. To eliminate false decisions by V_{ac} malformations, a three-consecutive-period mechanism is proposed. In VM, the positive peak V_{ACDIV} should be lower than V_{RV2C} for three consecutive periods to allow VM-to-RCM transitions; for RCM-to-VM transitions, the positive peak V_{ACDIV} should be higher than V_{RV2C} for three consecutive detections.

Typically, in VM, the proper input power detection should be done with open-circuit V_{ac} detection, which is challenging with open-loop rectifiers due to the distorted V_{ac}. However, the proposed SMDOR can leverage the operational state S_{VM3} to monitor the full-swing amplitude of V_{ac}, where the L_2–C_2

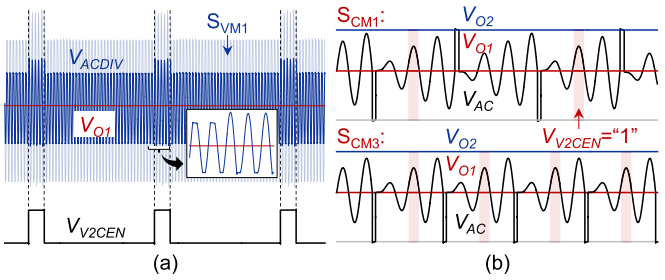

Fig. 13. Mode detection triggers. (a) VM 40p-5p triggers in S_{VM1}. (b) RCM triggers.

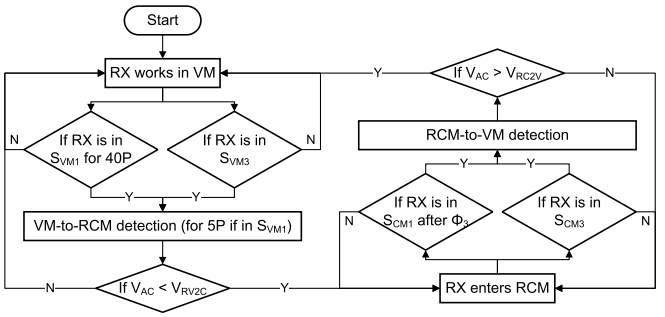

Fig. 14. Mode detector workflow.

tank freewheels during the positive half period of V_{ac}. This technique is named quasi-open-circuit V_{ac} detection. However, using S_{VM3} is not always feasible when the input weakens because SMDOR needs to hold up both the outputs, which necessitates mode-transition detection in S_{VM1}. Therefore, a 40p-5p detection trigger in S_{VM1} is proposed, as shown in Fig. 12(b). This mechanism enables SMDOR to temporarily operate in S_{VM3} for five resonance periods (P_0) after operating in S_{VM1} for 40 × P_0. Fig. 13(a) displays the waveforms of 40p-5p detection triggers. During the temporary S_{VM3}, C_{O1} can still be charged to maintain both the outputs without obvious voltage undershoots.

In RCM, the resonance phases, Φ_1, can be leveraged to detect the open-circuit V_{ac} without interfering with power delivery. Fig. 12(c) shows the mode detection trigger in RCM. Since the RCM mainly operates under weak coupling and the coupling changes slowly, the second P_0, instead of the first, in Φ_1 is selected for V_{ac} amplitude detection for higher accuracy. Moreover, Φ_1 starts with a negative or positive half cycle depending on whether it is followed by Φ_2 or Φ_3, respectively. The different starting half cycles result in different positive peak V_{ac} values. To exclude this error, the mode detection is only activated in Φ_1 followed by Φ_3, as shown in Fig. 13(b). A comprehensive workflow of the proposed mode detector is shown in Fig. 14.

C. Power Switch Gate-Driving Chain

Fig. 15 shows the detailed gate-driving chain for M_P. The gate control signal, V_{GP}, comes from both the VM and RCM switching controllers, depending on V_{MODE} and V_{CTP}. The VM switching controller includes an active-diode comparator, CMP_{VM}, and adaptive delay compensation loops. The

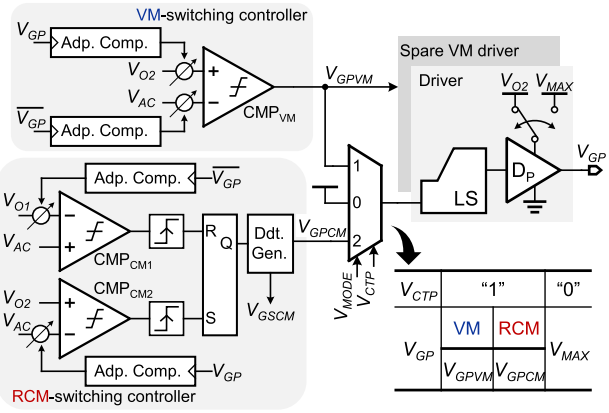

Fig. 15. M_P gate-driving chain including VM and RCM controllers, adaptive delay compensation blocks, and drivers.

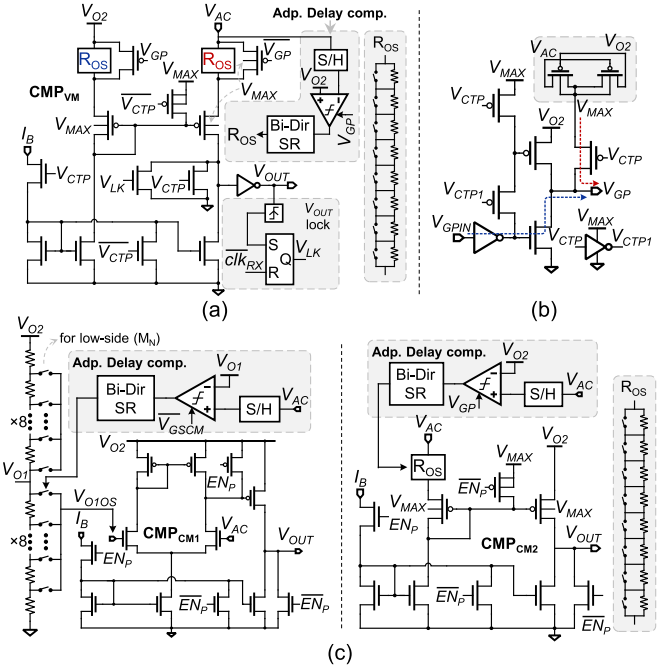

Fig. 16. M_P gate-driving chain implementations. (a) VM switching controller. (b) D_P. (c) Sub-blocks in the RCM switching controller.

RCM switching controller mainly involves two comparators, CMP_{CM1} and CMP_{CM2}, determining the start and end moments of the charging phases respectively, both of which also have adaptive delay compensation. The spare VM driver engages in VM for the full-size M_P. The gate-driving chain for M_N is implemented similarly.

Fig. 16 shows sub-block implementations in the M_P gate-driving chain. As depicted in Fig. 16(a), CMP_{VM} is implemented by a common-gate comparator with resistor-based turn-on/-off voltage offsets (R_{OS}). The adaptive delay compensation loop includes a sample-and-hold (S/H) circuit, a low-offset latched comparator, and an 8-bit bi-directional shift register. The S/H circuit samples V_{ac} at the final switching moments of V_{GP}, which is compared with V_{O2} to identify the switching errors. The shift register finally adjusts the two R_{OS} to achieve zero-voltage soft switching. As shown in Fig. 16(b),

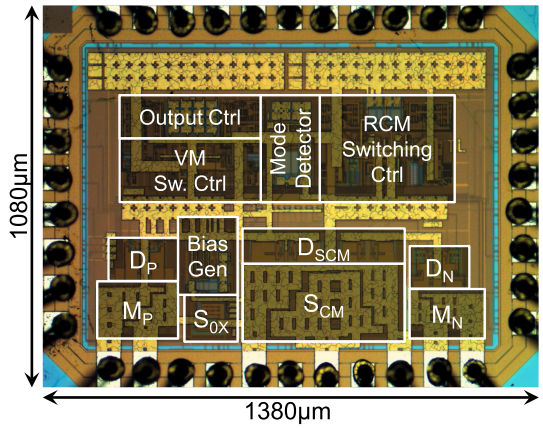

Fig. 17. Chip micrograph of SMDOR.

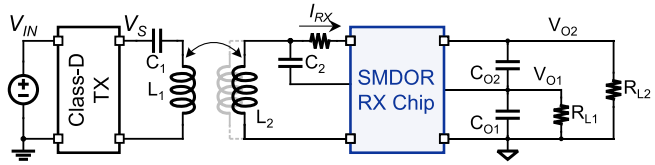

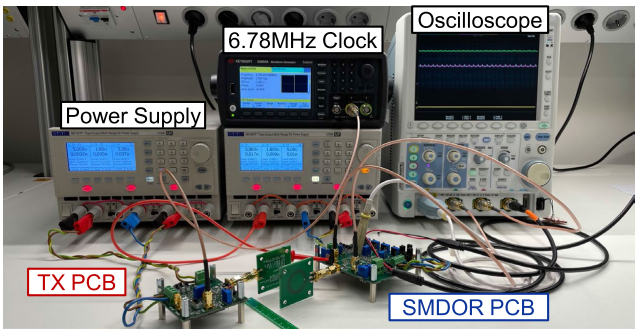

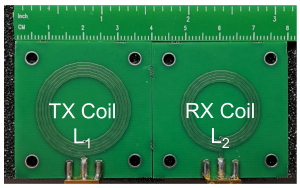

6.78MHz Link		
RX	L_2 540nH	Q_{L2} 83
	r_{L2} 11.5mm	C_2 1nF
TX	L_1 951nH	Q_{L1} 96.5
	r_{L1} 13.5 mm	C_1 560pF

Fig. 18. Measurement setup of SMDOR.

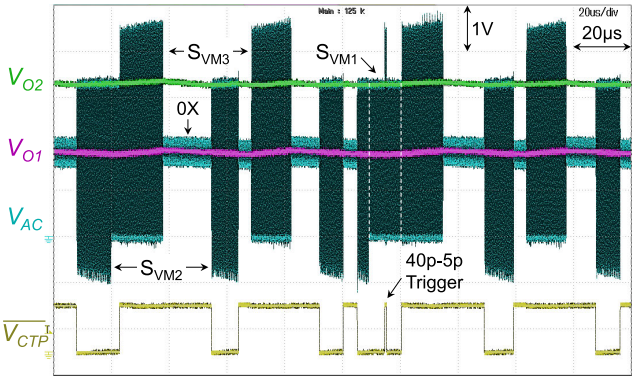

Fig. 19. Measured steady-state waveform of SMDOR in VM/0X at V_{O1} = 1.8 V, V_{O2} = 3.3 V, and $R_{L1} = R_{L2}$ = 1 kΩ.

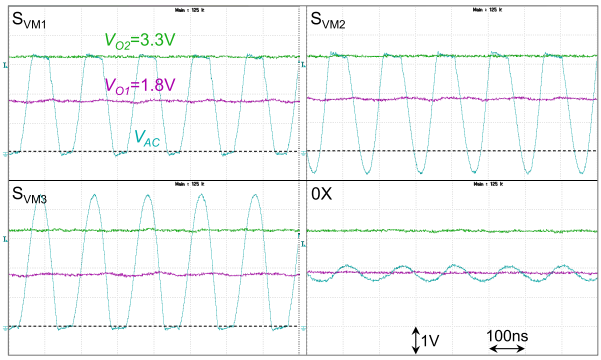

Fig. 20. Measured zoomed-in waveform of SMDOR in VM.

the gate driver of M_P, D_P, has two modes depending on V_{CTP}; V_{GP} follows either V_{GPIN} in VM/RCM or V_{MAX} in 0X mode. Fig. 16(c) details the RCM switching controller. CMP_{CM1} is implemented by a two-stage common-source comparator with an adaptive delay compensation loop similar to that in CMP_{VM}. The referred voltage V_{O1OS} at the negative node of CMP_{CM1} is adjusted to minimize the error between V_{ac} and V_{O1} at the final turn-off edge of S_{CM} (M_P's turn-on is a dead time later). CMP_{CM2} is implemented by a common-gate comparator with a resistor-based offset, R_{OS}, added on V_{ac}. The adaptive delay compensation loop adjusts R_{OS} to find the zero-voltage turn-off of M_P (S_{CM}'s turn-on is a dead time later).

IV. Measurement Results

The proposed SMDOR chip is fabricated in a 180-nm CMOS technology, occupying a silicon area of 1.5 mm^2 including pads, or 0.7 mm^2 excluding pads, as shown in Fig. 17. The 5-V devices are used in the power stage, and the 1.8-V devices are used in the control circuitry. Fig. 18 shows the measurement setup. C_{O1} and C_{O2} are implemented off-chip with 2.2-μF capacitance for each. The TX is realized by a 6.78-MHz half-bridge class-D power amplifier with a 3.3-V dc supply. Both TX and RX coils are assembled by single-layer planer PCB coils with 35-μm copper thickness. L_1 and L_2 have inductance of 951 and 540 nH, respectively. The coil separation distance between L_1 and L_2 is adjustable without lateral misalignment.

Fig. 19 shows the measured steady-state waveform of the proposed SMDOR when it regulates two outputs by alternately operating in three VM states and the 0X mode, under $R_{L1} = R_{L2}$ = 1 kΩ and strong coupling conditions. It is observed that V_{O1} and V_{O2} are regulated at 1.8 and 3.3 V, respectively. A 40p-5p mode detection trigger is presented when SMDOR operates in S_{VM1}. Fig. 20 shows the measured zoomed-in waveforms of the three VM states and the 0X mode. As described in Section II-B, V_{ac} shows freewheeling behavior in both S_{VM2} and S_{VM3}, and the 0X mode displays a minimum V_{ac} swing by shorting the L_2–C_2 resonance. It is also observed that adaptive delay compensation helps SMDOR realize near-optimal zero-voltage turn-on and -off of both M_P and M_N in all VM states.

Fig. 21 exhibits the measured steady-state waveform when the SMDOR operates in RCM/0X, under $R_{L1} = R_{L2}$ = 10 kΩ and weak coupling conditions. It is observed that

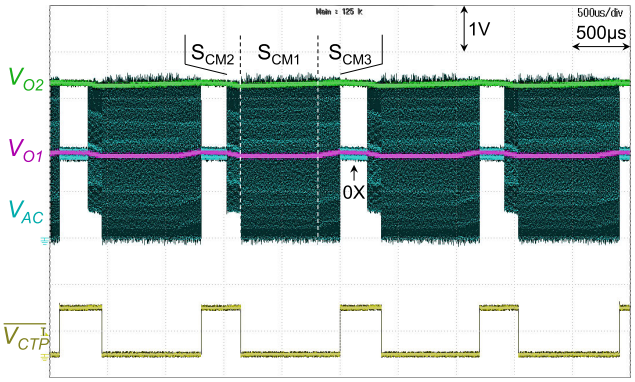

Fig. 21. Measured steady-state waveform of SMDOR in RCM/0X at V_{O1} = 1.8 V, V_{O2} = 3.3 V, and R_{L1} = R_{L2} = 10 kΩ.

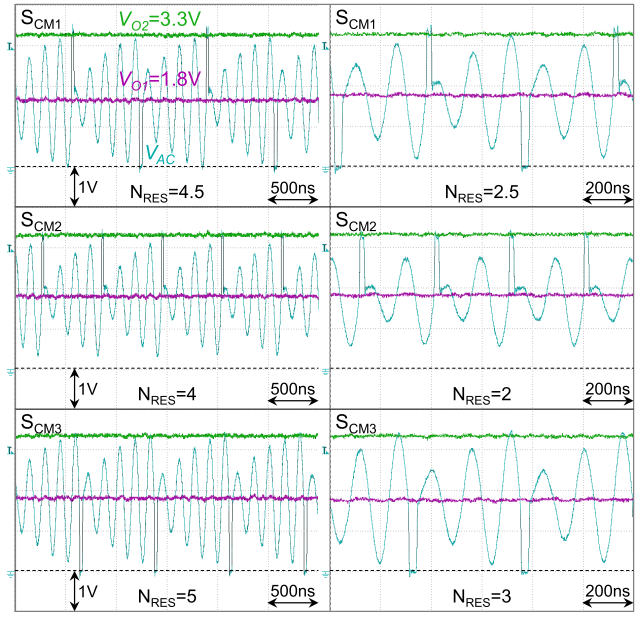

Fig. 22. Measured zoomed-in waveform of SMDOR in RCM under very weak (left) and weak (right) coupling conditions.

SMDOR still tightly regulates V_{O1} and V_{O2} at 1.8 and 3.3 V, respectively, by entering different RCM states. Fig. 22 shows the measured zoomed-in waveforms of RCM states under two different weak coupling conditions. Both the cases match the operation described in Section II-B. In the very weak coupling case, SMDOR has longer resonance phases (larger N_{RES}) to sufficiently build up energy. Adaptive delay compensation also helps SMDOR in RCM achieve near-optimal phase switching between resonance phases and charging phases.

Fig. 23 displays the load-transient waveform of SMDOR under R_{L1} steps between 5 kΩ and 180 Ω at R_{L2} = 700 Ω. SMDOR operates in VM/0X due to the strong coupling. The 0X mode engages more under R_{L1} = 5 kΩ condition, while S_{VM3} dominates when R_{L1} becomes heavier. During the transient, V_{O1} and V_{O2} are stably regulated at 1.8 and 3.3 V, respectively, without notable overshoot, undershoot, or cross-regulation, thanks to the hysteresis-based PPFM strategy. Fig. 24 shows the load-transient waveform of SMDOR in VM/0X under R_{L2} steps between 5 kΩ and 400 Ω at R_{L1} = 800 Ω. No undershoot/overshoot on V_{O2} or cross-regulation at V_{O1} is observed. Since R_{L2} extracts energy from both C_{O1}

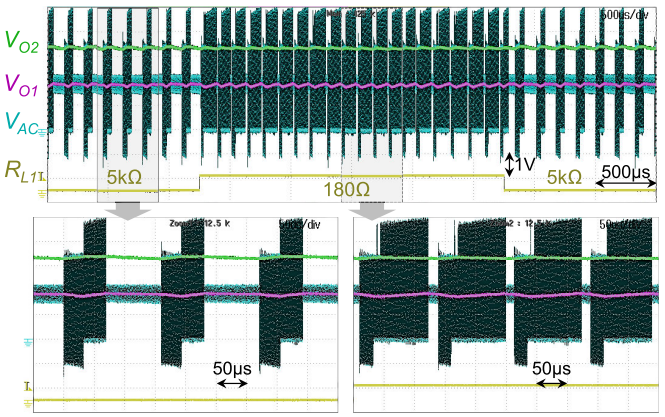

Fig. 23. Measured R_{L1}-load-transient waveform of SMDOR at V_{O1} = 1.8 V, V_{O2} = 3.3 V, R_{L2} = 700 Ω, and R_{L1} between 5 kΩ and 180 Ω.

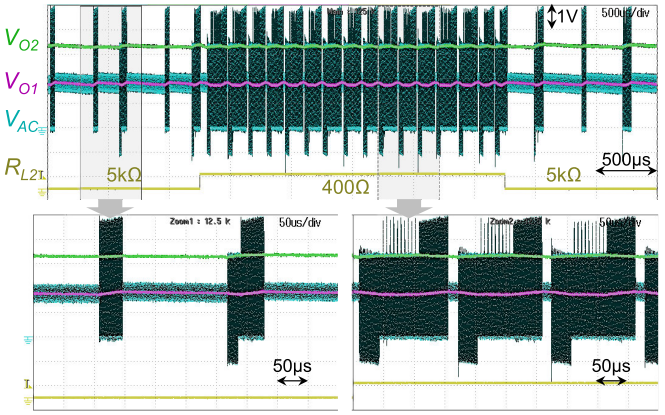

Fig. 24. Measured R_{L2}-load-transient waveform of SMDOR at V_{O1} = 1.8 V, V_{O2} = 3.3 V, R_{L1} = 800 Ω, and R_{L2} between 5 kΩ and 400 Ω.

and C_{O2}, SMDOR stays in S_{VM1} longer in the heavier loading case of R_{L2} = 400 Ω. Multiple 40p-5p mode detection triggers can be observed during S_{VM1} without obvious voltage drops at V_{O2}.

Fig. 25 presents the measured mode-transition waveform of SMDOR against TX power transients to demonstrate the efficacy of the proposed switching-mode operation, at D_{12} = 3.5 cm and R_{L1} = R_{L2} = 10 kΩ. The class-D power amplifier is switched from its full-power mode to a low-power mode by skipping three consecutive positive pulses. Thus, the TX emitting power is decreased by 4×, mimicking a strong-to-weak coupling transient. By manually delaying the VM-to-RCM transition, the voltage undershoots at both V_{O1} and V_{O2} are observed after the TX mode transient when SMDOR operates in VM. In comparison, when SMDOR switches to RCM, both V_{O1} and V_{O2} can be recovered and then stay in the normal regulation states. This proves the higher power receiving ability and the higher VCR of the RCM operation compared with the VM counterpart. Note that in the proposed SMDOR, the intentional VM-to-RCM delay does not exist and the dedicated mode detector completely avoids such a transient undershoot.

Fig. 26 exhibits the measured real-time mode-transition waveform of SMDOR at R_{L1} = R_{L2} = 10 kΩ. Seamless mode transition between VM and RCM is observed to regulate both V_{O1} and V_{O2} at 1.8 and 3.3 V, respectively, against coil separa-

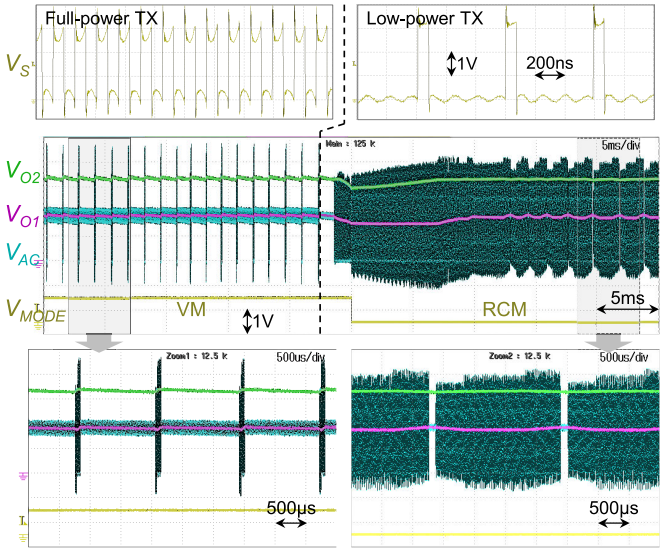

Fig. 25. Measured mode-transition waveform of SMDOR against TX power transients at $D_{12} = 3.5$ cm, $V_{O1} = 1.8$ V, $V_{O2} = 3.3$ V, and $R_{L1} = R_{L2} = 10$ kΩ, with manually delayed VM-to-RCM transition.

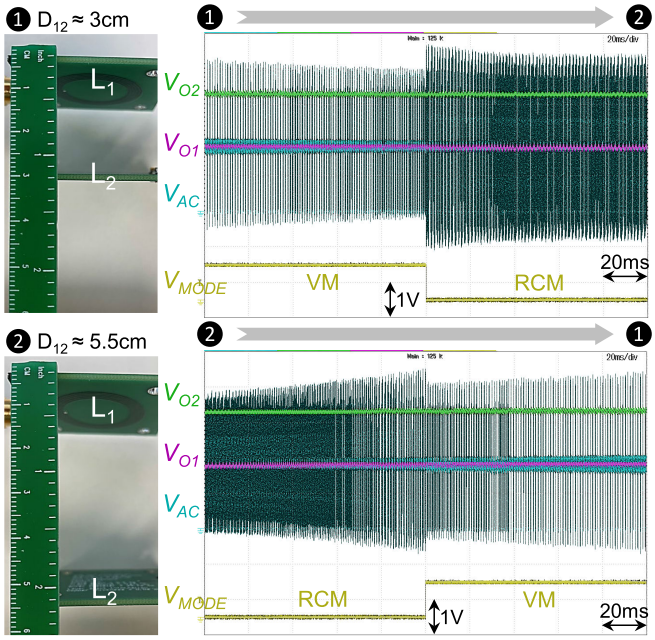

Fig. 26. Measured real-time mode-transition waveform of SMDOR against coil separation distance transients at $V_{O1} = 1.8$ V, $V_{O2} = 3.3$ V, and $R_{L1} = R_{L2} = 10$ kΩ.

tion distance transients between 3 and 5.5 cm. No undershoot voltage or mode dead zone is observed, benefiting from the proposed quasi-open-circuit mode detection.

The improved link adaptability of the proposed switching-mode operation is further quantitatively illuminated in Fig. 27, which shows the relationship between the output voltages and coil separation distance. When $R_{L1} = R_{L2} = 50$ kΩ, the conventional VM-only operation cannot sustain the two outputs when D_{12} exceeds 5.3 cm. In comparison, the fully activated SMDOR can sustain the two outputs until D_{12} reaches 7.5 cm, resulting in a 42% WPT range extension. Moreover, under the load conditions of $R_{L1} = R_{L2} = 10$ kΩ and $R_{L1} = R_{L2} = 5$ kΩ, the proposed SMDOR can still show WPT range extensions of 33% and 30%, respectively.

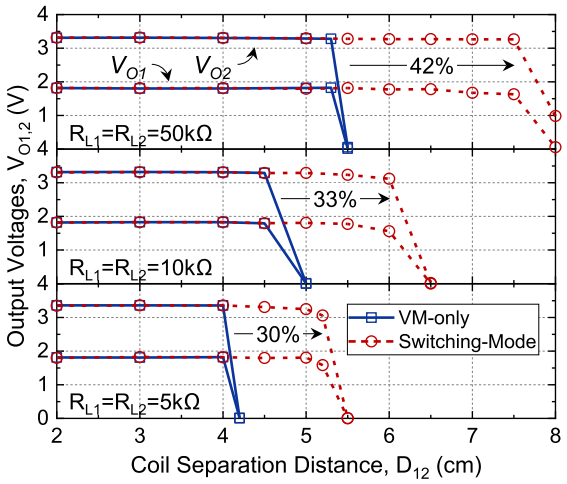

Fig. 27. Measured output voltages under different coil separation distances and load conditions.

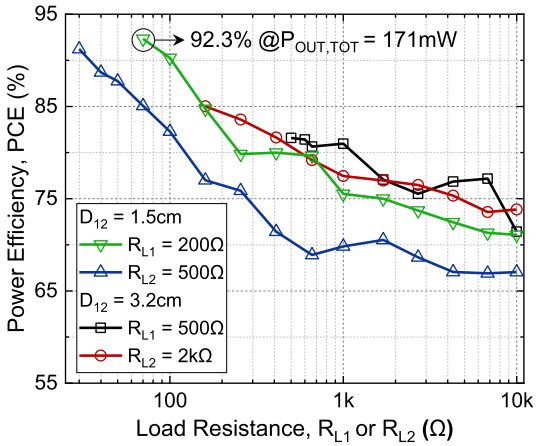

Fig. 28. Measured PCE under different load conditions and coil separation distances when SMDOR is in VM.

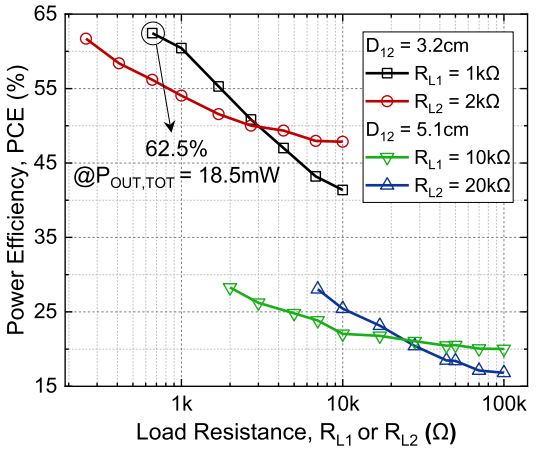

Fig. 29. Measured PCE under different load conditions and coil separation distances when SMDOR is in RCM.

Fig. 28 shows the measured PCE of the proposed SMDOR under different load conditions. In both $D_{12} = 1.5$ cm and $D_{12} = 3.2$ cm cases, SMDOR operates in VM. The output power is the sum of the power consumed in both the load resistances, while the input power is the product of V_{ac} and

TABLE II
COMPARISON TO STATE-OF-THE-ART WORKS

	JSSC'23 [18]	JSSC'24 [22]	JSSC'16 [25]	JSSC'20 [26]	JSSC'17 [29]	JSSC'24 [32]	This work
Technology	180nm	180nm	180nm	180nm	350nm	180nm	**180nm**
Frequency	6.78MHz	6.78MHz	0.05MHz	13.56MHz	1MHz	13.56MHz	**6.78MHz**
Topology	Full-bridge rectifier	Full-bridge rectifier	Parallel-LC RCM rectifier	Series-LC RCM rectifier	Half-bridge rectifier	Voltage doubler	**Dual-output voltage doubler**
Number of power switches	7	6	2	2	3	3	**3**
Number of Outputs (Voltages)	2 (3.7V, 5V)	2 (1-4.5V, 4.5V)	1 (unregulated)	1 (unregulated)	1 (3.2V)	1 (1.8V)	**2 (1.8V, 3.3V)**
Output Regulation	PFM	PWM	No	No	Reverse Current	DPWM	**PPFM**
Load-transient Over/undershoot	Unnoticeable	N/R	N/A	N/A	N/R	110mV	**Unobservable**
Soft Switching	Yes	No	No	Yes	No	Yes	**Yes**
Operation Mode	VM	VM	RCM	RCM	VM & RCM	VM & RCM	**VM & RCM**
Mode Transition					with dead zone	with 200mV undershoots	**Seamless**
Coil Diameter / Inductance (TX; RX)	32mm / 1.89µH; 31mm / 1.87µH	1.27 µH; 374 nH	6.5µH; 7.2mH	N/R	17cm / 250µH; 3cm / 4.4µH	3cm / 1.39µH; 2cm / 295nH	**2.7cm / 951nH; 2.3cm / 540nH**
Maximum WPT Distance	3mm	10mm	8.5cm	N/R	13.5cm	7.2cm	**7.5cm**
Max. $P_{OUT,TOT}$	300mW	123mW	2.8µW	15.4mW	20mW	81mW	**171mW**
Peak PCE	91.8%	92.7%	67.7%	92.6%	77%	90.1%	**92.3%**

N/R: not reported; N/A: not applied.

the current flowing into the SMDOR chip (I_{RX} in Fig. 18). A measured peak PCE of 92.3% is achieved when the total output power, $P_{OUT,TOT}$, reaches 171 mW, which is also the measured maximum power. The measured PCE of SMDOR in RCM is shown in Fig. 29. Table II shows comparison of this work with the recently published WPT RX works. The proposed SMDOR improves the link adaptability with RCM while maintaining the state-of-the-art PCE and delivered power of VM counterparts. A 7.5-cm maximum WPT distance is achieved using 2.7/2.3-cm-diameter TX/RX coils. Seamless mode transition is further enabled together with dual-output regulation, making it a competitive candidate for advanced biomedical applications.

V. CONCLUSION

This article presents a 6.78-MHz link-adaptive SMDOR for over 100-mW biomedical WPT applications. The switching-mode principle is modeled and verified by simulations and measurements. The prototype chip exhibits seamless mode transition between VM and RCM, up to 42% extended WPT range, high delivered power, high power efficiency, and dual-output regulation.

REFERENCES

[1] J. T. Robinson, J. E. Woods, and K. Yang, "25.3 toward exponential growth of therapeutic neurotechnology," in *IEEE Int. Solid-State Circuits Conf. (ISSCC) Dig. Tech. Papers*, vol. 67, Feb. 2024, pp. 426–428.

[2] M. Kiani, B. Lee, P. Yeon, and M. Ghovanloo, "12.7 a power-management ASIC with Q-modulation capability for efficient inductive power transmission," in *IEEE Int. Solid-State Circuits Conf. (ISSCC) Dig. Tech. Papers*, Feb. 2015, pp. 1–3.

[3] H. Kim, Y. Park, C. Sung, J. Cho, S. Park, and C. Kim, "DiTTO: A distance adaptive over 100-mW wireless power transfer system with 1.695-Mb/s uplink telemetry and a shared inductor two-output regulating rectification," *IEEE J. Solid-State Circuits*, vol. 59, no. 8, pp. 2568–2580, Aug. 2024.

[4] W. Wang et al., "Omnidirectional wireless power transfer for millimetric magnetoelectric biomedical implants," *IEEE J. Solid-State Circuits*, vol. 59, no. 11, pp. 3599–3611, Nov. 2024.

[5] D.-H. Yao, T.-N. Liu, M. Takamiya, and P.-H. Chen, "A 6.78-MHz wireless power transfer system with dual-output resonant current-mode regulating rectifier and transmission power regulation," *IEEE Trans. Circuits Syst. I, Reg. Papers*, vol. 70, no. 12, pp. 4986–4998, Dec. 2023.

[6] H.-S. Lee, K. Eom, and H.-M. Lee, "27.3 a 90.8%-efficiency SIMO resonant regulating rectifier generating 3 outputs in a half cycle with distributed multi-phase control for wirelessly-powered implantable devices," in *IEEE Int. Solid-State Circuits Conf. (ISSCC) Dig. Tech. Papers*, Feb. 2024, pp. 448–450.

[7] Y. Jia, S. A. Mirbozorgi, P. Zhang, O. T. Inan, W. Li, and M. Ghovanloo, "A dual-band wireless power transmission system for evaluating mm-sized implants," *IEEE Trans. Biomed. Circuits Syst.*, vol. 13, no. 4, pp. 595–607, Aug. 2019.

[8] G. L. Barbruni, C. Cordara, M. Carminati, S. Carrara, and D. Ghezzi, "A frequency-switching inductive power transfer system for wireless, miniaturised and large-scale neural interfaces," *IEEE Trans. Biomed. Circuits Syst.*, vol. 18, no. 3, pp. 679–690, Jun. 2024.

[9] M. G. P. Prez-Nicoli and F. Silveira, *Inductive Links for Wireless Power Transfer: Fundamental Concepts for Designing High-Efficiency Wireless Power Transfer Links*. Cham, Switzerland: Springer, 2021.

[10] K. Schuylenbergh and R. Puers, *Inductive Powering*. New York, NY, USA: Springer, 2009.

[11] Y. Lu, M. Huang, L. Cheng, W.-H. Ki, U. Seng-Pan, and R. P. Martins, "A dual-output wireless power transfer system with active rectifier and three-level operation," *IEEE Trans. Power Electron.*, vol. 32, no. 2, pp. 927–930, Feb. 2017.

[12] M. Kim, H.-S. Lee, J. Ahn, and H.-M. Lee, "A 13.56-MHz wireless power and data transfer system with current-modulated energy-reuse back telemetry and energy-adaptive voltage regulation," *IEEE J. Solid-State Circuits*, vol. 58, no. 2, pp. 400–410, Sep. 2022.

[13] S.-U. Shin, M. Choi, S. Jung, H.-M. Lee, and G.-H. Cho, "A time-interleaved resonant voltage mode wireless power receiver with delay-based tracking loops for implantable medical devices," *IEEE J. Solid-State Circuits*, vol. 55, no. 5, pp. 1374–1385, May 2020.

[14] R. Erfani, F. Marefat, and P. Mohseni, "A dual-output single-stage regulating rectifier with PWM and dual-mode PFM control for wireless powering of biomedical implants," *IEEE Trans. Biomed. Circuits Syst.*, vol. 14, no. 6, pp. 1195–1206, Dec. 2020.

[15] J. Tang, L. Zhao, and C. Huang, "A wireless hysteretic controlled wireless power transfer system with enhanced efficiency and dynamic response for bioimplants," *IEEE J. Solid-State Circuits*, vol. 58, no. 4, pp. 1160–1171, Aug. 2022.

[16] Z. Luo, J. Liu, and H. Lee, "30.9 a 90%-efficiency 40.68MHz single-stage dual-output regulating rectifier with ZVS and synchronous PFM control for wireless powering," in *IEEE Int. Solid-State Circuits Conf. (ISSCC) Dig. Tech. Papers*, Feb. 2023, pp. 454–456.

[17] T. Lu and S. Du, "A single-stage regulating voltage-doubling rectifier for wireless power transfer," *IEEE Solid-State Circuits Lett.*, vol. 6, pp. 29–32, 2023.

[18] F.-B. Yang, D.-H. Yao, and P.-H. Chen, "A quad-mode structure-reconfigurable regulating rectifier with shared-inductor DC–DC energy recycling in a wireless power receiver," *IEEE J. Solid-State Circuits*, vol. 59, no. 2, pp. 574–582, Feb. 2024.

[19] L. Cheng, W.-H. Ki, and C.-Y. Tsui, "A 6.78-MHz single-stage wireless power receiver using a 3-mode reconfigurable resonant regulating rectifier," *IEEE J. Solid-State Circuits*, vol. 52, no. 5, pp. 1412–1423, May 2017.

[20] J. Lin, Y. Lu, C. Zhan, and R. P. Martins, "A single-stage dual-output regulating rectifier with hysteretic current-wave modulation," *IEEE J. Solid-State Circuits*, vol. 56, no. 9, pp. 2770–2780, Sep. 2021.

[21] H.-M. Lee, H. Park, and M. Ghovanloo, "A power-efficient wireless system with adaptive supply control for deep brain stimulation," *IEEE J. Solid-State Circuits*, vol. 48, no. 9, pp. 2203–2216, Sep. 2013.

[22] H.-S. Lee and H.-M. Lee, "A 92.7%-efficiency 6.78-MHz energy-resuscitating resonant regulating rectifier with dual outputs for wirelessly powered devices," *IEEE J. Solid-State Circuits*, vol. 59, no. 10, pp. 3204–3217, Oct. 2024.

[23] T. Lu, K. A. A. Makinwa, and S. Du, "A single-stage dual-output regulating voltage doubler for wireless power transfer," *IEEE J. Solid-State Circuits*, vol. 59, no. 9, pp. 2922–2933, Sep. 2024.

[24] X. Li, C.-Y. Tsui, and W.-H. Ki, "Power management analysis of inductively-powered implants with 1X/2X reconfigurable rectifier," *IEEE Trans. Circuits Syst. I, Reg. Papers*, vol. 62, no. 3, pp. 617–624, Mar. 2015.

[25] M. Choi, T. Jang, J. Jeong, S. Jeong, D. Blaauw, and D. Sylvester, "A resonant current-mode wireless power receiver and battery charger with -32 dBm sensitivity for implantable systems," *IEEE J. Solid-State Circuits*, vol. 51, no. 12, pp. 2880–2892, Dec. 2016.

[26] S.-W. Hong, "A resonant current-mode wireless power and data receiver for loosely coupled implantable devices," *IEEE J. Solid-State Circuits*, vol. 55, no. 12, pp. 3200–3209, Dec. 2020.

[27] H. S. Gougheri and M. Kiani, "Current-based resonant power delivery with multi-cycle switching for extended-range inductive power transmission," *IEEE Trans. Circuits Syst. I, Reg. Papers*, vol. 63, no. 9, pp. 1543–1552, Sep. 2016.

[28] T. Lu and S. Du, "A 3-Phase resonant current-mode wireless power receiver with residual-free energy delivery and digital-assisted ZVS achieving 94.5% efficiency," in *Proc. IEEE Custom Integr. Circuits Conf. (CICC)*, Apr. 2024, pp. 1–2.

[29] H. S. Gougheri and M. Kiani, "Self-regulated reconfigurable voltage/current-mode inductive power management," *IEEE J. Solid-State Circuits*, vol. 52, no. 11, pp. 3056–3070, Nov. 2017.

[30] H. S. Gougheri and M. Kiani, "A self-regulated voltage/current-mode integrated power management with seamless mode transition and extended input-voltage range," in *Proc. IEEE Custom Integr. Circuits Conf. (CICC)*, Apr. 2018, pp. 1–3.

[31] H. Sadeghi Gougheri and M. Kiani, "An inductive voltage-/current-mode integrated power management with seamless mode transition and energy recycling," *IEEE J. Solid-State Circuits*, vol. 54, no. 3, pp. 874–884, Mar. 2019.

[32] T. Lu and S. Du, "A coupling-adaptive wireless power transfer system with voltage-/current-mode receiver and global digital-PWM regulation," *IEEE J. Solid-State Circuits*, vol. 59, no. 12, pp. 4175–4187, Dec. 2024.

[33] T. Lu and S. Du, "27.4 a 13.56MHz wireless power transfer system with hybrid voltage-/current-Mode receiver and global digital-PWM regulation achieving 150% transfer range extension and 72.3% end-to-end efficiency," in *IEEE Int. Solid-State Circuits Conf. (ISSCC) Dig. Tech. Papers*, Feb. 2024, pp. 450–452.

[34] T. Lu and S. Du, "A switching-mode single-stage dual-output regulating rectifier achieving 92.33% efficiency and extended range for wireless power transfer," in *Proc. IEEE Eur. Solid-State Electron. Res. Conf. (ESSERC)*, Sep. 2024, pp. 169–172.

[35] M. Taghadosi and H. Kassiri, "A real-time-link-adaptive operation scheme for maximum energy storage efficiency in resonant CM wireless power receivers," *IEEE Trans. Circuits Syst. I, Reg. Papers*, vol. 68, no. 1, pp. 510–523, Jan. 2021.

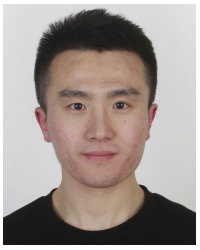

Tianqi Lu (Graduated Student Member, IEEE) received the B.Sc. degree in physics from Nanchang University, Nanchang, China, in 2018, and the M.Sc. degree in integrated circuit engineering from Tsinghua University, Beijing, China, in 2021. He is currently pursuing the Ph.D. degree with the Department of Microelectronics, Delft University of Technology, Delft, The Netherlands.

He has authored several peer-reviewed publications in IEEE JOURNAL OF SOLID-STATE CIRCUITS, *Solid-State Circuits Letters* (SSCL), International Solid-State Circuits Conference (ISSCC), and Custom Integrated Circuits Conference (CICC). His research interests include power management/mixed-signal integrated circuits for wireless power transfer systems, dc–dc power converters, and biomedical applications.

Dr. Lu was a recipient of the 2025 ISSCC Student Travel Grant Award (STGA) selected by the Solid-State Circuits Society (SSCS). He served as a reviewer for IEEE TRANSACTIONS ON CIRCUITS AND SYSTEMS—I: REGULAR PAPERS, IEEE TRANSACTIONS ON CIRCUITS AND SYSTEMS—II: EXPRESS BRIEFS, and IEEE TRANSACTIONS ON POWER ELECTRONICS.

Sijun Du (Senior Member, IEEE) received the B.Eng. degree (Hons.) in electrical engineering from University Pierre and Marie Curie (UPMC), Paris, France, in 2011, the M.Sc. degree (Hons.) in electrical and electronic engineering from Imperial College, London, U.K., in 2012, and the Ph.D. degree in electrical engineering from the University of Cambridge, Cambridge, U.K., in January 2018.

He worked at the Laboratoire d'Informatique de Paris 6 (LIP6), UPMC, and then as an IC Engineer at Shanghai, China, from 2012 to 2014. He was a Post-Doctoral Researcher at the University of Cambridge, in October 2014. He was a Summer Engineer Intern at Qualcomm Technology Inc., San Diego, CA, USA, in 2016. He was a Post-Doctoral Researcher at the Department of Electrical Engineering and Computer Sciences (EECS), University of California, Berkeley, CA, USA, from 2018 to 2020. In 2020, he joined the Department of Microelectronics, Delft University of Technology (TU Delft), Delft, The Netherlands, as an Assistant Professor. His current research is focused on energy-efficient integrated circuits and systems, including power management integrated circuits (PMIC), energy harvesting, wireless power transfer, and dc/dc converters used in the Internet-of-Things (IoT) wireless sensors, wearable electronics, and biomedical devices.

Dr. Du received the Dutch Research Council (NWO) Talent Program VENI Grant in the 2021 round, the Best Student Paper Award in IEEE ICECS 2022, and the SSCS Reviewer Award in 2024. He serves as the IEEE ICECS Sub-Committee Chair in 2022 and 2024, respectively, the IEEE International Solid-State Circuits Conference (ISSCC) Student Research Preview (SRP) Committee Member since 2023, and the IEEE ISCAS Sub-Committee Chair in 2025.